J. Fluid Mech. (1997), *vol.* 341, *pp.* 245–267. Printed in the United Kingdom

Dynamics of inviscid capillary breakup: collapse and pinchoff of a film bridge

By Y.-J. CHEN[1] AND P. H. STEEN[1,2]

[1]School of Chemical Engineering, Cornell University, NY 14853, USA

[2]Center for Applied Mathematics, Cornell University, NY 14853, USA

(Received 7 October 1996 and in revised form 10 January 1997)

An axisymmetric film bridge collapses under its own surface tension, disconnecting at a pair of pinchoff points that straddle a satellite bubble. The free-boundary problem for the motion of the film surface and adjacent inviscid fluid has a finite-time blowup (pinchoff). This problem is solved numerically using the vortex method in a boundary-integral formulation for the dipole strength distribution on the surface. Simulation is in good agreement with available experiments. Simulation of the trajectory up to pinchoff is carried out. The self-similar behaviour observed near pinchoff shows a 'conical-wedge' geometry whereby both principal curvatures of the surface are simultaneously singular – lengths scale with time as $t^{2/3}$. The similarity equations are written down and key solution characteristics are reported. Prior to pinchoff, the following regimes are found. Near onset of the instability, the surface evolution follows a direction dictated by the associated static minimal surface problem. Later, the motion of the mid-circumference follows a $t^{2/3}$ scaling. After this scaling 'breaks', a one-dimensional model is adequate and explains the second scaling regime. Closer to pinchoff, strong axial motions and a folding surface render the one-dimensional approximation invalid. The evolution ultimately recovers a $t^{2/3}$ scaling and reveals its self-similar structure.

1. Introduction

In capillary-driven breakup of a fluid body, surface tension drives a nonlinear pinching of the interface that ultimately breaks the body into two or more pieces. Examples include water dripping from a tap, the breakup of a liquid jet into droplets, the generation of an emulsion by shearing and the collapse of a liquid bridge. Understanding of the physics of breakup is incomplete, especially when the driven flow is inviscid. Collapse of a film bridge is a particularly attractive prototype for study since (i) breakup begins and ends at an equilibrium state, (ii) the same fluid is on both sides of the moving interface, (iii) there is no complication of imposed motion (e.g. jets and emulsions) and (iv) the breakup is easily realized in the laboratory. By its self-similarity, the pinchoff behaviour is likely to be prototypical of any breakup for which capillarity is balanced by fluid inertia (Peregrine, Shoker & Symon 1990).

Self-similar pinchoff behaviour is important to engineering computation. In such computation, typically a necking element is tracked until the radius of the pinch decreases below some arbitrary tolerance, at which instant the element is declared 'broken'. With a self-similar solution to hand, the computations can be terminated in a natural way by matching in the region of overlap with the self-similar behaviour.

Pinchoff behaviour is also important for its physical implications. Most significant, perhaps, is the translational motion of the pinch point. Although pinchoff occurs at a fixed pair of points along the axis, the surface has an unbounded axial acceleration at the pinch instant. In a real system, the corresponding concentration of force may be disruptive or even destructive.

Our computations are motivated by observations of the axisymmetric collapse of a soap-film bridge. The initial film surface is a 'sleeve-like' bridge (a catenoid), supported by two coaxial circular end supports – connected but not simply connected in topology. Because of its finite extent, there is a path for air to move from inside to outside during collapse. The dynamics of the collapse involves the inviscid flow of air driven by capillarity. After collapse, the film consists of two planar pieces that span the end supports with, possibly, additional disconnected components (e.g. satellite bubble(s)). Observations are reported in Cryer & Steen (1992).

Surface tension deforms the interface, displacing a mass of air. On dimensional grounds, sufficiently close to pinchoff, the radius at the neck d must depend on time t through tension σ and air density ρ as $\tau^{2/3}$,

$$d = (\sigma\tau^2/\rho)^{1/3}, \tag{1.1}$$

where

$$\tau \equiv (t_p - t) \tag{1.2}$$

is time measured from the pinchoff time t_p. Such scaling is well-known and the basis for the similarity solution constructed by Keller & Miksis (1983). They solved for the planar motion of a wedge (initially) of inviscid fluid (semi-infinite) driven by its bounding capillary surface and embedded in a passive environment. The wedge tip (initial configuration) may be interpreted as a pinch point, with the similarity solution giving the ensuing motion. The dynamical law (1.1) must hold regardless of whether the problem is planar or three-dimensional. On the other hand, the shape at pinchoff will depend strongly on dimension of the embedding space. This is a consequence of pinchoff being driven by the principal curvatures through the mean curvature (via the Young–Laplace law). For a surface of revolution (curve $r(s), z(s)$), the principal curvatures are

$$\kappa_1 = z'/r, \tag{1.3}$$

$$\kappa_2 = r'z'' - r''z', \tag{1.4}$$

where $' = \mathrm{d}/\mathrm{d}s$ and s denotes arclength ($r'^2 + z'^2 = 1$). For planar configurations, the curvature is given by κ_2 with r replaced by Cartesian coordinate y, say. In that case, a quiescent far field is compatible with an interface that diverges at infinity provided y is a linear function of z – the wedge. In the axisymmetric case, a diverging interface and a quiescent far field are incompatible. Indeed, in three dimensions, even a pressure field that decays as $1/r$ requires a velocity field with weaker decay and a potential that diverges. The only tube-like shape with zero mean curvature in three dimensions is the catenoid which exists only for finite length. It is clear, therefore, that an axisymmetric *global* similarity solution like that of Keller & Miksis, but for pinchoff, is not possible. On the other hand, a self-similar pinching solution matched to a weak flow in the far field may be possible. Indeed, this is what our computations show.

Analyses of axisymmetric pinching have assumed a radial scale much smaller than the axial length scale (e.g. Meseguer 1983). Keller (1983) constructs similarity solutions using such a slenderness (long-wave) assumption with overall mass and momentum

balances. The scaling exponent is left undetermined. Ting & Keller (1991), Keller, King & Ting (1995) and Papageorgiou (1995*a*) follow a similar approach to obtain a set of one-dimensional equations to describe pinchoff. See Papageorgiou (1995*a*) for a review of the literature and an account of distinctions among these analyses. One consequence of the slenderness assumption can be complete neglect of curvature κ_2. Some analyses include weak versions of κ_2 (e.g. Schulkes 1993), but a common feature of predictions of one-dimensional models based on slenderness is that this assumption is violated before pinchoff is reached (e.g. Papageorgiou 1995*b*). In contrast, when viscosity is present, κ_1 goes to infinity before κ_2 and there is self-consistency of the one-dimensional models (Eggers 1993; Eggers & Dupont 1994; Shi, Brenner & Nagel 1994). The state of understanding of inviscid pinchoff, therefore, is somewhat unsatisfactory.

The present study is based on a computation of the trajectory of a surface up to the pinchoff instant. Experiments that track the motion of a collapsing soap film motivate the study. However, sufficiently close to pinchoff, an inviscid description will ultimately be inappropriate since the Reynolds number based on radial fluid velocity ultimately vanishes (it scales as $\tau^{1/3}$ according to relation (1.1)). In other words, our mathematical model cannot be expected to be faithful to the experiment very near to pinchoff. On the other hand, it may well be that the 'chunk of physics' neglected by the inviscid model is not crucial to the behaviour before and after pinchoff. In much the same way, most previous studies assume a continuum (implicitly or explicitly) while close enough to pinchoff the continuum hypothesis must be violated. In this case the neglected chunk of physics occurs on the molecular length scales. For our inviscid model and, in fact, the broader class of continuum models of pinchoff, it is likely that useful predictions will emerge in spite of what is neglected. Our comparison of the inviscid model with experiment below shows that the model is indeed faithful over a significant regime of the collapse. Certain pinchoff features, such as the size of the satellite bubble, are also well-predicted by the model.

The governing equations for the dynamical evolution of the surface may be written as a system of integro-differential equations via a boundary-integral formulation. The dipole form of the integral representation is adopted and numerical solution uses the vortex method. The method has been previously applied to study nonlinear wave dynamics (Baker, Meiron & Orszag 1982), for example, and breakup of a unstable liquid bridge (Mansour & Lundgren 1990). A feature of our numerical calculation is the solution for the shape and velocity field directly for a non-planar configuration. A more typical computation, in contrast, delivers the velocity potential which then must be numerically differentiated to obtain the velocity field. Direct computations for vortex sheet shape have been restricted to planar configurations as far as we are aware.

Various stages of collapse may be identified from experiment, as sketched in figure 1. Collapse begins at a neutrally stable equilibrium. Instability of the initial state is triggered by ambient disturbances. The ensuing trajectory consists of three stages: necking, breaking and relaxing (Cryer & Steen 1992). The 'necking' stage lasts until the film breaks. Breaking includes pinchoff, the singularity in space–time that changes the topology of the configuration. The 'breaking' stage is defined to be a temporal neighbourhood of pinchoff, extending over the entire film. In contrast, the pinchoff singularity may be local in space. 'Relaxing' starts when the film disconnects and lasts until the final equilibrium state is reached. Attention in this paper is restricted to the necking stage and the breaking stage up to the pinchoff singularity.

Necking may be subdivided into 'primary' and 'secondary' necking, according to

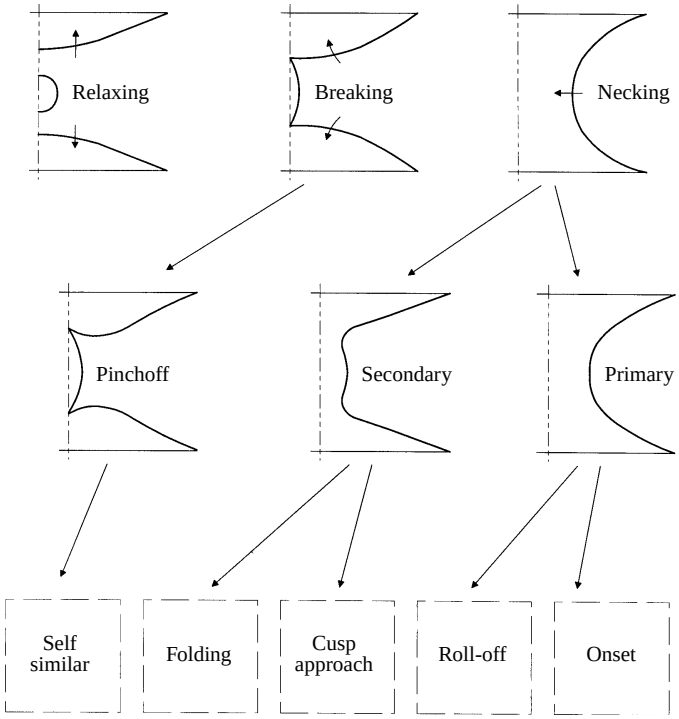

FIGURE 1. Catalogue of regimes characterizing the collapse trajectory. The schematic shapes are distinguished from experiment. The boxed regimes are distinguished by power law by the simulation.

the number of necks (figure 1). Primary necking lasts as long as the minimum radius remains at midplane – i.e. as long as there is only one neck. As pressure builds at the mid-axis stagnation point, the mid-plane minimum becomes a maximum and two secondary minima move symmetrically away, deepening as they move, much like a bifurcation. Secondary necking lasts from the birth of the two secondary minima until their simultaneous pinchoff. The double pinch seals off a satellite bubble in the middle and disconnects the film at two points equidistant from the mid-axis.

Our computations identify the following subregimes (figures 1 and 2). Within primary necking, 'onset' is characterized by algebraic growth of infinitesimal disturbances, to be contrasted with the exponential growth more typical of hydrodynamic instabilities. This growth arises due to the cubic nature of the local energy surface at the turning point in the curve of equilibria. Beyond onset, but still within the primary necking stage, a subregime of 'apparent' $\tau^{2/3}$ collapse of the neck diameter d is observed. This is not a true self-similar behaviour but an artifact of the mid-plane position where there is no axial velocity, by symmetry. We refer to this subregime as 'roll-off'. It ends as stagnation pressure builds at the mid-axis, decelerating the inward motion.

Secondary necking also shows a subregime of apparent similarity behaviour (figure 2): κ_2 grows as ${\kappa_1}^2$ and consequently a vertical tangent develops. In particular, $\kappa_1 \propto \tau^{-2/5}$ and $\kappa_2 \propto \tau^{-4/5}$. The different rates of collapse signal cusp formation. For this reason, we refer to this subregime as 'cusp-approach'. Since the radius is not zero at this vertical tangent, it cannot correspond to pinchoff. A parametric description of the curve allows the computation to continue beyond the infinite slope. It is found that passage through this behaviour occurs via 'fold-over'. Ultimately, a state of 'true'

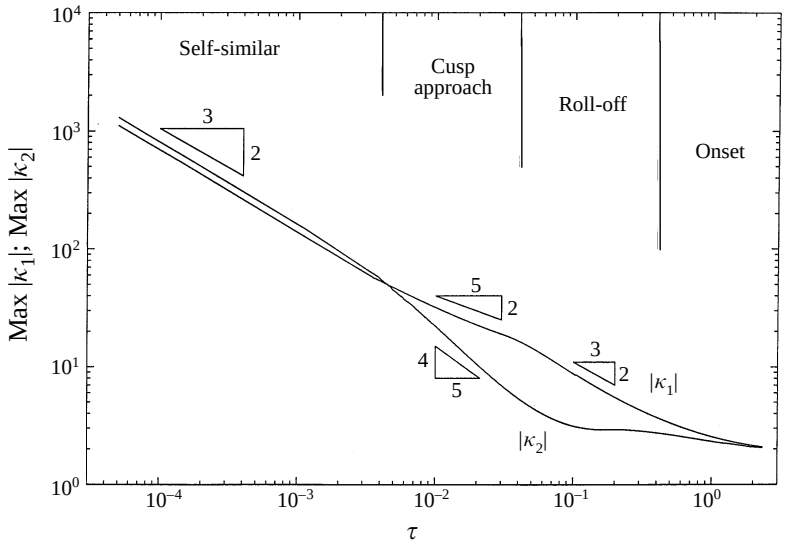

FIGURE 2. Time sequences of the maximum principal curvatures during collapse. Note that between roll-off and cusp-approach the location of the maxima shifts from mid-plane to secondary minima.

self-similarity is reached – where the principal radii collapse in unison, at the rate $\tau^{2/3}$.

The paper is organized as follows. First, as background, the state-space of steady solutions (equilibria) is briefly reviewed. The dynamical problem is then formulated and the numerical approach along with its validation is described. Results are then reported in order of the subregimes observed, as outlined above: onset, roll-off, cusp-approach, fold-over, and self-similarity. We close with a discussion and summary.

2. Background

Here, we provide the essential observations and predictions of static equilibria. A more detailed account of experiment, classical theory, and the good agreement between the two can be found in Cryer & Steen (1992).

2.1. *Experiment*

A soap film may be stretched between two circular rings (coaxial and equal radius, say) to form a tubular bridge, as long as the separation distance L of the endrings is small relative to the radius R (figure 3). Experiments, following classical studies of Plateau (1863), show that, at a critical length, the bridge abruptly collapses, breaking up into pieces (Cryer 1990; Steen 1992; Cryer & Steen 1992). After collapse, there remain two principal pieces: flat circular disks of film that span each of the end supports. Throughout collapse the film maintains a symmetry about its mid-plane (mirror-symmetry) and about its axis of revolution (axisymmetry).

The stages of breakup have been summarized in §1. The entire event occurs in less than 10^{-1} s. It is extremely reproducible. The experiments use a soap film made from oleic acid according to a classical recipe (Plateau 1863). Each film bridge is allowed to drain beforehand to a thickness on the order of 1 μm. This is sufficiently thin that gravity has negligible influence throughout the collapse (Bond number $\ll 1$). The

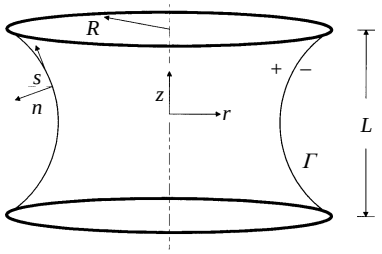

FIGURE 3. Defining sketch for the bridge.

appropriate time scale is

$$T \equiv (\rho R^3/\sigma)^{1/2} \approx 1.1 \times 10^{-2}\text{s}.$$

This estimate for the time for surface tension to overcome the inertia of the air ρR^3 is comparable to that observed in the experiments ($R = 1.9$ cm, $\sigma = 60$ dyne cm^{-1}, and $\rho = 1.2 \times 10^{-3}$ g cm^{-3}). T will be used to scale time in the analysis below. As pointed out above, the viscosity of the air must ultimately dominate inertia during a $\tau^{2/3}$ pinchoff. On the other hand, for our experiments, the inertia of the soap film comes into play first. The assumption of a mathematical surface in the model is the first to break down. Table 1 shows a comparison of T with the time scales for the various effects not included in the model. The predictions of the model are expected to deviate from the experiments due to film inertia at $\tau \approx 10^{-2}T$. This estimated τ is obtained from figure 2 after finding the curvature $1/d$ at which air and film inertia are the same order.

It is important to distinguish the 'modelling question' from the 'mathematical question'. The modelling questions asks, 'what physics dominates the experimental behaviour and what is an appropriate mathematical model of that behaviour?' The mathematical question asks, 'given a particular mathematical model, what does it predict?' The film is modelled as a mathematical surface endowed with constant tension and the motion of the surface drives an irrotational flow in an unbounded environment. Our focus is on the mathematical question. Nevertheless, it turns out that model predictions are faithful to experiment over much of the collapse (i.e. up to $\tau \approx 10^{-2}T$) and that some post-pinchoff characteristics are well-predicted.

2.2. *States of equilibrium*

The film is modelled as a surface of revolution. Classical states of static equilibrium can be obtained as the extremals of an energy functional. The free energy is proportional to the surface area – the constant of proportionality is the film tension. The surface area functional can be written

$$J[h] \;=\; \int_{-L/2}^{L/2} h \left\{ 1 + \left(\frac{\mathrm{d}h}{\mathrm{d}z} \right)^2 \right\}^{1/2} \mathrm{d}z \tag{2.1}$$

with a suitable classes of shape functions as domain, $h(z) \in \mathbf{C}^1[-L/2, L/2]$, $h(\pm L/2) = R$.

The functional has regular extremals given by the 'catenary' (Euler 1774). The one-parameter family (parameter a) is given by

$$\frac{h(z)}{R} \;=\; a \cosh\left(\frac{z}{aR} \right). \tag{2.2}$$

	Time scales	Values (s)
Air inertia	$(\rho R^3/\sigma)^{1/2}$	1×10^{-2}
Film inertia	$(\rho_f R^2 \delta/\sigma)^{1/2}$	4×10^{-3}
Air viscosity	$\mu R/\sigma$	6×10^{-6}
Film viscosity	$\mu_f \delta/\sigma$	5×10^{-8}

TABLE 1. Time scales of various physical effects in experiments. Here, evaluation uses air viscosity $\mu = 1.8 \times 10^{-4}$ g cm^{-1} s^{-1}, film thickness $\delta = 1\,\mu$m, film density $\rho_f = 1.0$ g cm^{-3}, and film viscosity $\mu_f = 3.0 \times 10^{-2}$ g cm^{-1} s^{-1}. Other values are given in the text.

These are the connected solutions of the Euler–Lagrange equation (Young–Laplace equation in this context). Stability of the catenary can be determined by classical methods, that is, by the Legendre condition and the conjugate point condition derived from the second variation (Howe 1887; Gillette & Dyson 1971), or by a more modern approach that exploits the variational structure (Maddocks 1987; Lowry & Steen 1995). It is well known that, for a fixed radius, there exist two distinct equilibria for a bridge length $\ell \equiv L/R < \ell_c \equiv 1.325$, and no connected equilibria for $\ell > \ell_c$. In the language of bifurcation theory, the nonlinear problem has a turning-point bifurcation at $\ell = \ell_c$. The solution with lower surface energy is a local minimum of the free energy surface (stable) and the one with higher energy is a saddle point (unstable). There are also disconnected solutions of the Euler–Lagrange equations. Of particular interest is the two-component solution consisting of two planar circles. These have an energy somewhat less than the catenoid at $\ell = \ell_c$ (about 10 % less) and exist for all values of ℓ. The collapse trajectory is the sequence of non-equilibrium states that takes the system from the catenoid to the disconnected equilibrium state.

Dimensional considerations place strong restrictions on the pinchoff singularity. Assuming that surface tension drives an inviscid flow, the observed neck diameter d (or any response with dimension of length) can depend on two groups only, one time-like and the other an aspect ratio, say

$$d/R = f(\sigma\tau^2/\rho R^3, \ell). \tag{2.3}$$

For all the computations of this paper, $\ell = \ell_c$ is fixed. Sufficiently close to the pinchoff singularity, the macroscopic length scale R cannot play a role, and therefore the response (2.3) must reduce to that in equation (1.1). Self-similarity defines the pinchoff regime.

3. Formulation

A mathematical surface, denoted Γ, spans the two endrings $\partial\Gamma$ (figure 3). Cylindrical coordinates are employed and arclength s is measured in the positive z-direction. The rate of change of the unit tangent $\boldsymbol{s}$ is in the normal direction $\boldsymbol{n}$. The principal curvatures are given by (1.3), (1.4). Note the two special cases where axial and azimuthal slices give the principal curvatures. At $r' = 0$ ($z' = 1$), an axial tangent to the plane curve, the principal curvatures are simply $(1/r, -r'')$, while for $z' = 0$ ($r' = 1$), a radial tangent, they are simply $(0, z'')$.

During collapse the surface displaces a volume of air. There are no sources of vorticity. The flow field is assumed irrotational. The Bernoulli equation gives the pressure within the flow. Across the singular surface, the jump of pressure is balanced

by the mean curvature, according to the Young–Laplace equation, which yields,

$$\left[\frac{\partial\phi}{\partial t}+\tfrac{1}{2}|\nabla\phi|^2\right] = -\frac{\sigma}{\rho}(\kappa_1+\kappa_2) \quad \text{on} \quad \Gamma \tag{3.1}$$

where $[\cdot] \equiv (\cdot)^+ - (\cdot)^-$. Here, ϕ represents the velocity potential that satisfies the Laplace equation in the fluid region

$$\nabla^2\phi = 0.$$

The normal velocity across the moving surface must be continuous

$$(\boldsymbol{n}\cdot\nabla\phi)^+ = (\boldsymbol{n}\cdot\nabla\phi)^- \quad \text{on} \quad \Gamma. \tag{3.2}$$

For a bounded surface, assuming that ϕ is bounded and decays fast enough at infinity, classical potential theory shows that the boundary integral equation for dipole distribution $\mu(\boldsymbol{x},t) \in \mathbf{C}^{1,\alpha}(\Gamma,\mathbf{R})$ automatically satisfies the kinematic condition (3.2) and, therefore, is a preferred representation:

$$\phi(\boldsymbol{x}^\star) = -\int_\Gamma \boldsymbol{n}(x)\cdot\nabla G(\boldsymbol{x};\boldsymbol{x}^\star)\mu(\boldsymbol{x})\mathrm{d}\boldsymbol{x}. \tag{3.3}$$

Here, $G(\boldsymbol{x};\boldsymbol{x}^\star) = 4\pi/|\boldsymbol{x}-\boldsymbol{x}^\star|$ is the free-space Green's function. A velocity is defined on the interface by

$$\boldsymbol{v}(\boldsymbol{x},t) \equiv ((\nabla\phi)^+ + (\nabla\phi)^-)/2. \tag{3.4}$$

It then follows directly from (3.3) that

$$\boldsymbol{v}(\boldsymbol{x}^\star,t) = -\int_\Gamma \boldsymbol{n}(x)\cdot\nabla^\star\nabla G(\boldsymbol{x};\boldsymbol{x}^\star)\mu(\boldsymbol{x},t)\mathrm{d}\boldsymbol{x}, \tag{3.5}$$

where the integral exists as a principal value in the sense of (3.4) and, in particular, the normal component can be realized by the Hadamard 'finite part' (Hadamard 1923; Krishnasamy *et al.* 1990). An evolution equation for the dipole distribution function follows from (3.1) and (3.3) with some manipulation (Baker *et al.* 1982):

$$\dot{\mu}(\boldsymbol{x},t) = -(\kappa_1+\kappa_2), \tag{3.6}$$

where the dot denotes the Lagrangian time derivative with convective velocity (3.4).

The reformulated problem requires solution for dipole distribution $\mu(\boldsymbol{x},t)$ and shape $\boldsymbol{X}(t) \in \Gamma$ as a set of integro-differential equations for the motion of Lagrangian particles,

$$\begin{bmatrix}\dot{\mu}\\ \dot{\boldsymbol{X}}\end{bmatrix} = \begin{bmatrix}-(\kappa_1+\kappa_2)\\ \boldsymbol{v}\end{bmatrix}. \tag{3.7}$$

In this reformulation, the lengths have been scaled by the ring radius R, time by T, velocity potential and dipole strength by R^2/T, and pressure by σ/R. For the axisymmetric case we shall study, the surface integral can be reduced to a line integral by integrating the equation in the azimuthal direction analytically.

The boundary conditions are fixed endpoints with no vorticity generation there. It follows from (3.3) that

$$\phi^+ - \phi^- = \mu(\Gamma),$$
$$(\phi^+)' - (\phi^-)' = \mu'(\Gamma).$$

Hence the requirement of no generation of vorticity near the endrings (existence of a continuous velocity field) demands

$$\mu = \mu' = 0 \quad \text{at} \quad \partial\Gamma. \tag{3.8}$$

With this smoothness condition, definition of the integral (3.5) can be extended to $\partial\Gamma$.

The above system can be approximated by a set of ordinary differential equations through a numerical discretization scheme. Equation (3.6) is a Fredholm equation of the second kind; however, tedious procedures to solve the equation (for example, by iteration) can be avoided in this special case by choosing the surface marker points to coincide with the Lagrangian particles. By updating the surface shape $\boldsymbol{X}(t)$ and dipole distribution function $\mu(\boldsymbol{x}, t)$ through (3.7), the collapsing sequence can be constructed by tracing the trajectories of the marker points. The resulting numerical algorithm is then similar to the simulation of vortex dynamics. Details of the discretization are given next.

4. Computational approach

We discretize the surface by N Lagrangian particles $\boldsymbol{X}_i(t) \equiv (z_i(t), r_i(t))$, each of which has the dipole strength $\mu_i(t)$. The mean curvature is approximated by the 'circular arc' method (Pozrikidis 1992) and the dipole distribution between the marker points is approximated by linear interpolation. Once the mean curvature and the velocity of each particle are calculated, the sequence $\{\boldsymbol{X}_i, \mu_i\}_{i=1}^N$ will be updated by a modified Euler time-advancing scheme

$$\mu_i^{k+1} = \mu_i^k - (\kappa_1 + \kappa_2)^k \Delta t, \tag{4.1}$$

$$\boldsymbol{X}_i^{k+1} = \boldsymbol{X}_i^k + \boldsymbol{v}(\{\boldsymbol{X}_j^k, \mu_j^{k+1}\}_{j=1}^N)\Delta t, \tag{4.2}$$

with given initial conditions $\{\boldsymbol{X}_i^0, \mu_i^0\}_{i=1}^N$. Adaptive time step is used to control the maximal advancing distance of each particle to be within a prescribed limit. The technique of repositioning particles along the arclength is applied to prevent the particles from clustering or getting coarse. At regular intervals of time the particles are redistributed, with spacing adjusted by the rule

$$\Delta s \propto \exp(-|\kappa_2|^\lambda).$$

That is, particles are moved to regions of high curvature. The exponent $\lambda = 0.2$ is used in the current implementation. The convergence of the calculations is checked by increasing the number of particles in the simulation. It is observed that the results are virtually indistinguishable for $N > 81$.

The integral (3.5) has a regular and (hyper)singular part. Integration of regular parts on each discretized segment employs a Gaussian quadrature routine (d01ahf in the NAG library) while the singular part is evaluated using identities such as

$$\lim_{\epsilon \to \pm 0} \int_{-a}^{b} \frac{\epsilon}{s^2 + \epsilon^2} \mathrm{d}s = \pm\pi, \qquad \lim_{\epsilon \to 0} \int_{-a}^{b} \frac{s^2 - \epsilon^2}{(s^2 + \epsilon^2)^2} \mathrm{d}s = -\frac{1}{a} - \frac{1}{b}, \qquad a, b > 0.$$

These arise in the limiting process whereby the marker point $\boldsymbol{X}_i$ approaches the surface from the fluid side (Gray & Sansoucie 1993). The advantage of direct evaluation of (3.5) is the added accuracy that comes with avoiding numerical differentiation of the velocity potential while the price is the difficulty of analytically handling the singularity of (3.5). In contrast to the milder singularity of (3.3), the structure of (3.5) is not well-documented.

It is necessary to impose the constraint (3.8) on the initial conditions so that the limiting procedure in the integral makes sense. The computations show that this regularization and repositioning procedure are two key aspects of the numerical

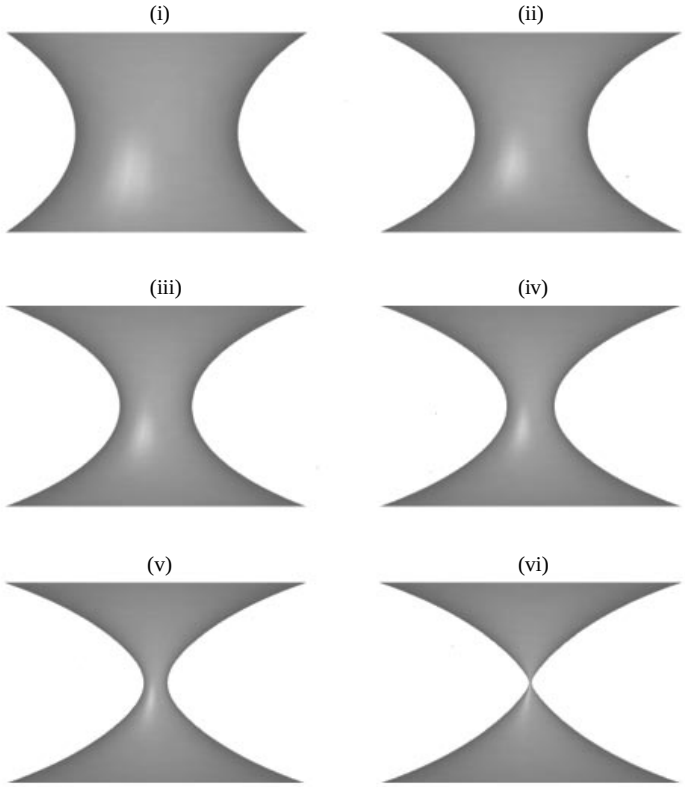

FIGURE 4. Evolution of the collapsing catenoid surface, according to the flow from mean curvature calculation: (i) $\tau = 8.570$; (ii) $\tau = 0.325$; (iii) $\tau = 0.0748$; (iv) $\tau = 0.0248$; (v) $\tau = 0.0048$; (vi) $\tau = 1.5 \times 10^{-4}$.

stability. Without the smoothness condition, discontinuity of the flow field itself would lead to erratic behaviour transmitted from the particles near the endrings; without repositioning the system would be too stiff (Hou, Lowengrub & Shelly 1994) to be integrated in acceptable time steps.

We test the numerical algorithm by simulating the oscillation of an inviscid drop suspended in a neutrally buoyant fluid. Linear analysis shows that the shape of the oscillating drop is perturbed off the spherical shape by spherical harmonics (Lamb 1932) with frequencies

$$\omega^2 = n(n-1)(n+1)(n+2)/(2n+1).$$

We implemented the numerical algorithm by exciting an axisymmetric shape perturbation with a single harmonic in constant-volume modes ($n \geqslant 2$). It is found that the numerical results agree well with the linear solutions as long as the initial amplitude $\varepsilon \equiv \|\boldsymbol{X}^0 - \boldsymbol{X}(\text{sphere})\|_\infty$ of the given perturbation is small ($\varepsilon \leqslant 0.05$), so that the nonlinear oscillations are not significant. The discrepancy, for example, in the oscillating frequency (to check the numerical diffusion and dispersion errors) for the excitation of $n = 2$ mode is within 0.2% for $\varepsilon = 0.05$, $N = 81$. The volume of the drop (to check the kinematic condition) is conserved to within 0.1% during the deformation.

To further test aspects of the algorithm and to illustrate computational demand, we calculate the evolution from the unstable catenoid according to flow by mean

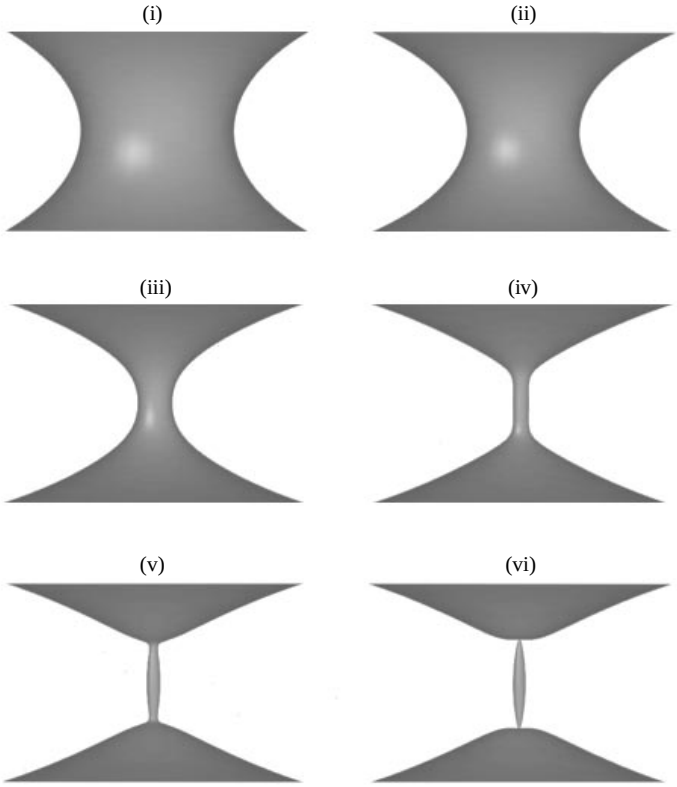

FIGURE 5. Evolution of the collapsing soap-film surface, according to the dipole simulation: (i) $\tau = 4.386$; (ii) $\tau = 0.873$; (iii) $\tau = 0.123$; (iv) $\tau = 0.0483$; (v) $\tau = 0.0283$; (vi) $\tau = 1.0 \times 10^{-4}$.

curvature (e.g. Chopp & Sethian 1991),

$$\boldsymbol{v} = -(\kappa_1 + \kappa_2)\boldsymbol{n}. \tag{4.3}$$

That is, we replace (3.5) by (4.3) and solve for the Lagrangian motion. The simple dynamical law (4.3) has no influence of inertia. The motion is governed solely by the local state of the surface. It has been used to test purely computational techniques of handling the breakup of a shape (e.g. level set method). Figure 4 shows the sequence of states computed via our algorithm ($N = 81$). These compare favourably with those of Chopp & Sethian (1991). The colliding time is estimated by extrapolation as r_{min} approaches zero. Shapes are labelled by different values of τ. There is a single pinch point and a collapse singularity that grows as $\tau^{1/2}$, as it must, by the law (4.3). The total computational time to pinchoff is 2 minutes, using a IBM RISC 6000 machine.

In contrast, figure 5 shows snapshots of the collapse according to (3.7) from the same initial state. One can see that, instead of touching at the equator ($z = 0$), the shape of the surface changes from concave to near-cylindrical in the middle. Two singularities appear, one on each side of the cylinder ($z_p \approx \pm 0.32$), and encapsulate a small blob at the centre. Also compare with the regimes sketched in figure 1, from experiment. The total computation time for this sequence is on the order of 18 hours, using the same IBM machine. Hence, these computations which take inertia into account (non-local dynamics) demand three orders of magnitude longer. A major proportion of computational time is devoted to accurate evaluation of the

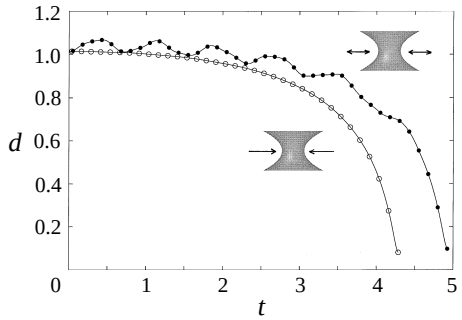

FIGURE 6. Time trajectories of the mid-plane diameter of the collapsing bridge. Data plotted start with different initial conditions: solid circles – random Fourier modes; open circles – the conjugate-point perturbation.

integral (3.5). For the most intensive calculations reported below (e.g. figures 10–12), $N = 1001$ is employed and the computational time required is an order of magnitude longer than that to obtain figure 5.

5. Onset of instability

The shapes during primary necking are single-valued functions of z and will be referred to as a function $r = h(z)$ in this section and the next.

Initial conditions are specified as a shape perturbation without initial velocity. That is, an initially homogeneous dipole distribution is assumed, which automatically satisfies the condition (3.8). Numerical experience shows that the distribution remains smooth near the fixed points as the surface deforms in time.

Since the governing physics is a conservative system, we expect oscillations or 'ringing' to be prevalent in solutions to (3.7). This is indeed the case. Most initial shapes lead to oscillations. A typical trajectory that plots the neck diameter versus time is shown in figure 6. The diameter executes a few periods of oscillation and then collapses with a monotone behaviour. The motion starts from an initial perturbation of the critical catenoid, $\bar{h}(z; a_c) = a_c \cosh(z/a_c)$, characterized by a truncated Fourier series with a restricted initial amplitude ($\Sigma \varepsilon_k \leqslant 0.05$),

$$h^0(z) \;=\; \bar{h}(z; a_c) + \sum_{k=0}^{M} \varepsilon_k \cos((2k+1)\pi z/\ell_c). \tag{5.1}$$

The time scale of the oscillation depends on the selection of $\{\varepsilon_k\}$. The oscillation is nearly independent of the discretization order (as long as $N > 41$) and hence is not a spurious phenomena.

In contrast, however, there is a special initial condition that leads the system to pinchoff without ringing (figure 6). This condition is related to the structure of the state-space for the static problem. The idea is simple. There is a preferred direction (perturbation) at the critical catenoid that corresponds to the steepest gradient down the energy surface. Mathematically, this is related to the conjugate-point condition of the variational problem. Recall that an eigen-solution of the Jacobi equation is given by

$$q(z) \;\equiv\; \frac{\partial}{\partial a}\bar{h}(z; a_c) \;=\; \cosh\left(\frac{z}{a_c}\right) - \frac{z}{a_c}\sinh\left(\frac{z}{a_c}\right). \tag{5.2}$$

This is the kernel of the second variation of the surface energy integral (Bliss 1946). It is *the* initial condition for which ringing is observed to be absent.

That the dynamical behaviour is influenced by the structure of the equilibrium state-space does not come as a surprise. On the other hand, since little has been reported about such an influence, we pause to examine it in a bit more detail. One of the results is the algebraic growth law for disturbances at onset of the instability.

Consider the Taylor expansion of $J[h]$ (see (2.1)) of the variation in the direction of $q(z)$,

$$J[\bar{h} + \varepsilon q] \sim J_0 + \frac{\varepsilon^3}{3!} J_0''', \quad J_0''' > 0. \tag{5.3}$$

Note that $J'(0) = J''(0) = 0$. The first derivative vanishes since $\bar{h}(z)$ is a stationary point and the second derivative vanishes due to the conjugate point condition. Equation (5.3) shows that the surface energy is a locally monotone function of ε. By analogy with the Hamiltonian dynamics of a conservative system, the system can be written as $K + J =$ constant, where K is the kinetic energy and J is viewed as the potential energy (see Dussan 1975 for interfacial systems). Suppose that, in the regime of small amplitude ε, the kinetic energy can be approximated by $c(\mathrm{d}\varepsilon/\mathrm{d}t)^2/2$, where c is a constant of proportionality and, for simplicity, the initial velocity is set to be zero. The Hamiltonian can then be written as

$$\frac{c}{2}\left(\frac{\mathrm{d}\varepsilon}{\mathrm{d}t}\right)^2 + \frac{\varepsilon^3}{3!} J_0''' \sim \frac{\varepsilon(0)^3}{3!} J_0''', \tag{5.4}$$

in which $\varepsilon(0)$ is the amplitude of the initial disturbance. The trajectory of $\varepsilon(t)$ can be obtained by integrating (5.4):

$$\varepsilon(t) \sim \varepsilon(0) - (4\varepsilon(0)^2 J_0'''/c)\, t^2, \qquad t \ll 1. \tag{5.5}$$

Note the monotonic growth of the instability – it is quadratic in nature.

In contrast, the general perturbation (5.1) will have components orthogonal to $q(z)$. These components will lead to the observed short-time oscillations. A three-dimensional analogy of the local potential surface shows a trough whose generator is a cubic curve (the direction q). For general initial conditions, the trajectory will oscillate back and forth while accelerating down the generator, attracted by the path of steepest descent. This acceleration is called 'roll-off' to bring to mind the 'marble-in-well' analogy. This finite-dimensional analogue is an adequate representation of the infinite-dimensional problem, at least locally, near the onset of instability. Note that the concept of 'time-to-collapse' needs modification for this inviscid model. Indeed, different initial conditions with the same amplitude can lead to collapse times that differ by 15% due to the oscillations (figure 6). Note, however, that starting the clock after the oscillations have 'accelerated away' will yield an unambiguous collapse time.

6. Roll-off

After onset, the surface accelerates into the 'roll-off' stage and then decelerates as the satellite bubble forms, marking the end of primary necking. The two principal radii of curvature at the mid-axis ($z = 0$), $r_1 \equiv |\kappa_1^{-1}|$ and $r_2 \equiv |\kappa_2^{-1}|$, are plotted versus τ during primary necking in figure 7 (logarithmic scale). The solid lines are the computations. The symbols represent data taken from high-speed video recording of the collapse. The radial radius $r_1 = r|_{z=0}$ can be measured directly from digitized images. On the other hand, the axial radius $r_2 = |-r''|^{-1}{}_{z=0}$ requires a calculation

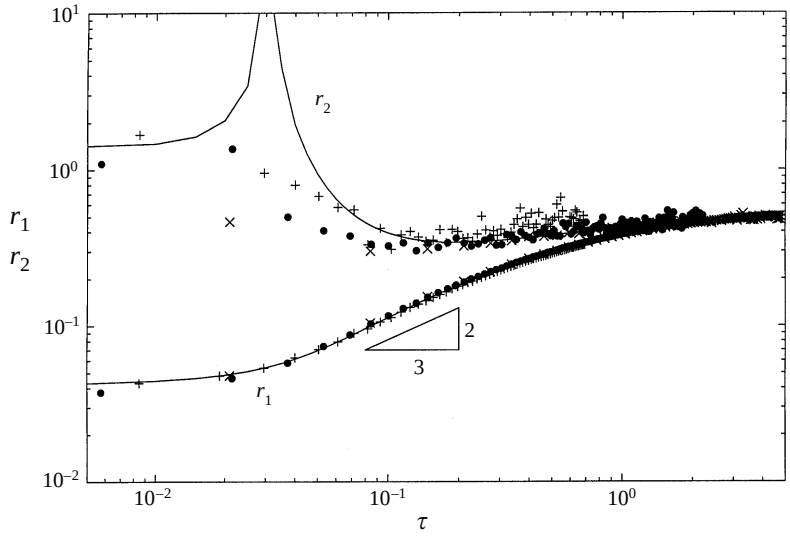

FIGURE 7. Roll-off. Principal radii of curvatures at the mid-plane section versus time. The solid curves represent the computations. The symbols represent the experimental data collected by a high-speed video. Symbols represent soap solutions of •, 10%; +, 20%; and ×, 40% glycerol (i.e. different soap-film viscosities).

of curvature from an image curve (i.e. differentiating data twice). The resulting data have significantly larger error bars and scatter as a result, as might be expected. The agreement with r_1, in particular, is seen to be good. Roll-off lasts for about a decade ($\tau = 0.4 \sim 0.04$) characterized by a nearly a 2/3-power-law correlation of r_1 with τ. The interface slows until the neck point of $h(z)$ shifts away from the midpoint.

Roll-off is an example of apparent scaling. For about a decade, the motion correlates without an external length. In particular, the trajectory of the neck seems 'not to be aware' of the ring radius R, according to

$$r_1^3 \approx 0.133\, \sigma\tau^2/\rho. \tag{6.1}$$

On the other hand, this scaling breaks as the pressure increases to form the satellite bubble. As a consequence, the size of the bubble depends on the ring radius. Indeed, it scales linearly with R. The equivalent radius of the satellite bubble from the numerical simulation is

$$R_{eq}/R \approx 0.067, \tag{6.2}$$

which compares favourably to experiment,

$$R_{eq}^{exp}/R \approx 0.06 \pm 0.005, \tag{6.3}$$

obtained via a straightforward measurement of the final bubble diameter for four different ring radii. Finite film thickness precludes comparison of the time trajectory of the soap film with simulation much beyond roll-off.

We argue that the observed scaling is special to the equator, due to the symmetry that requires zero axial velocity there. Consider a fluid packet near the equator. The kinetic energy is dominated by the radial acceleration and is driven by the radial curvature. The energy budget reads

$$\tfrac{1}{2}(\dot{h})^2 \approx 1/h,$$

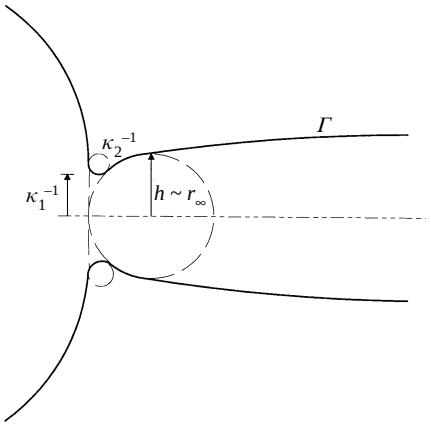

FIGURE 8. Schematic diagram for the 'cusp-approach' mechanism.

which gives a relationship $h \propto \tau^{2/3}$. This inward, radial movement results in strong axial motion inside the tube (by kinematics)

$$u \approx (-2\dot{h}/h)z.$$

A relatively high velocity potential $|\phi|$ is thereby gradually generated at the stagnation point (cf. the Bernoulli equation), thus retarding the equatorial surface movement. The portion of the surface nearby is flattened. This strong nonlinear interaction is analogous to what occurs in the breakup of a slender liquid bridge. Extensive studies have been devoted to satellite formations using various methods (e.g. Chaudhary & Redekopp 1980; Mansour & Lundgren 1990; Tjahjadi, Stone & Ottino 1992 for viscous fluid).

7. Cusp-approach

Secondary necking begins as the equator of the surface saturates at $r_\infty \approx 0.041$. The single minimum branches into two minima symmetric to the equator. These two minima accelerate downward leading to a double pinchoff. Near the secondary minima, the axial curvature κ_2 quickly increases by an order of magnitude until $O(\kappa_2) \sim O(\kappa_1)$. In this regime $|\kappa_2| \propto |\kappa_1|^2$. Figure 2 plots the time dependencies of $\max|\kappa_1|$ and $\max|\kappa_2|$. According to the computations, using a best fit over the decade ($\tau = 0.04 \sim 0.004$), the two principal curvatures blow up at the rates of

$$\kappa_1 \approx 4.5\tau^{-0.38}, \qquad \kappa_2 \approx -0.48\tau^{-0.83}. \tag{7.1}$$

The surface tends to form a 'cusp-like' singularity since $|\kappa_2|$ blows up faster than $|\kappa_1|$.

The observed scalings (7.1) can be explained simply. Figure 8 shows a schematic of the explanation. Consider a Lagrangian element on the surface in the pinching region. Since the axial momentum is driven by κ_2 near the minimum point ($|\partial\kappa_1/\partial z| \ll |\partial\kappa_2/\partial z|$), the equation of motion reads

$$\dot{u} \approx -(\partial/\partial z)\kappa_2. \tag{7.2}$$

Suppose that the local convective z-coordinate has length scale l and the minimal radius has scale r, then $|\kappa_2| \approx \partial^2 h/\partial z^2 \approx r/l^2$, and (7.2) leads to

$$\mathrm{d}^2 l/\mathrm{d}\tau^2 \approx -r/l^3. \tag{7.3}$$

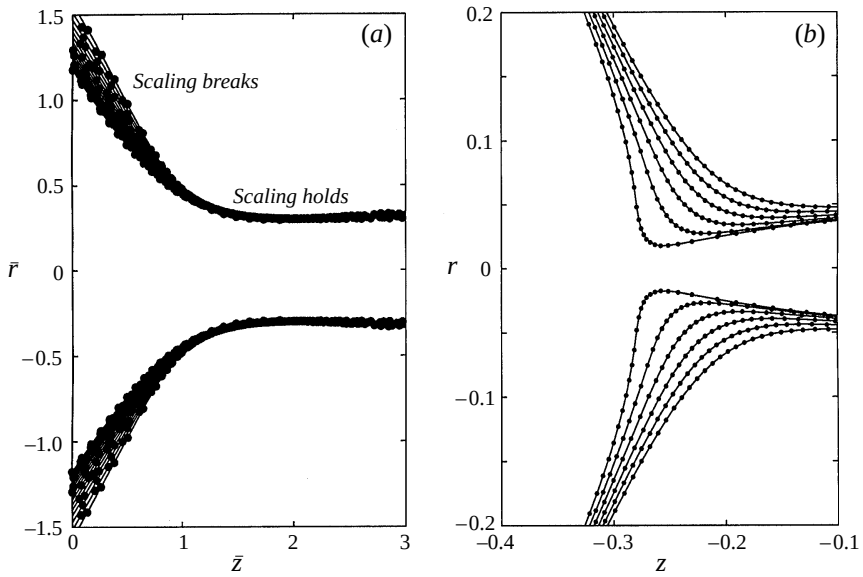

FIGURE 9. Cusp-approach regime. (*a*) Rescaled surface shape in the normalized coordinates (see text). (*b*) Surface shape evolution in the primitive coordinates. Solid circles represent grid points.

On the other hand, since $|\kappa_2| \propto |\kappa_1|^2$ and using the geometry shown in the schematic, $|\kappa_2|^{-1} \approx r^2/(4r_\infty)$, so that

$$l^2/r \approx r^2/4r_\infty. \tag{7.4}$$

Combining (7.3) and (7.4), one arrives at

$$\left.\begin{array}{ll} \kappa_1 \propto r_\infty^{-2/5}\,\tau^{-2/5}, & r \propto r_\infty^{2/5}\,\tau^{2/5}, \\ \kappa_2 \propto -r_\infty^{1/5}\,\tau^{-4/5}, & l \propto r_\infty^{1/10}\,\tau^{3/5}. \end{array}\right\} \tag{7.5}$$

This shows how the lengths depend on the external length scale r_∞. In this regime, the surface is virtually a thin tube contracting and pushing airflow out from its centre. We remark that Papageorgiou (1995*b*) had found similar scalings to (7.5) for a pinching slender jet in an analysis of a one-dimensional inviscid slice model.

The similarity variables suggested by (7.5) are

$$\bar{r} \equiv r/\tau^{2/5}, \quad \bar{z} \equiv (z - z_p)/\tau^{3/5}.$$

Using these, the computations for cusp-approach are plotted in figure 9(*a*). The scaling apparently holds for a while and then breaks close to the singularity in space–time. The scaling breaks due to fold-over as seen in a plot of the same computations in unscaled variables, figure 9(*b*).

8. Fold-over

Cusp-approach does not end in pinchoff since the minimum radius does not go to zero there. According to figure 2, scaling breaks at about $\tau \sim 0.004$ where fold-over occurs. There, the acceleration of κ_2 slows while κ_1 speeds up to yield $O(\kappa_2) \sim O(\kappa_1)$. Figure 10(*a*) plots a sequence of interface shapes for $\tau \leqslant 0.004$. The film surface has folded and is double-valued in r. The small-slope approximation is clearly violated. There is a reverse flow above the turning point (see figure 13). Therefore, an inviscid

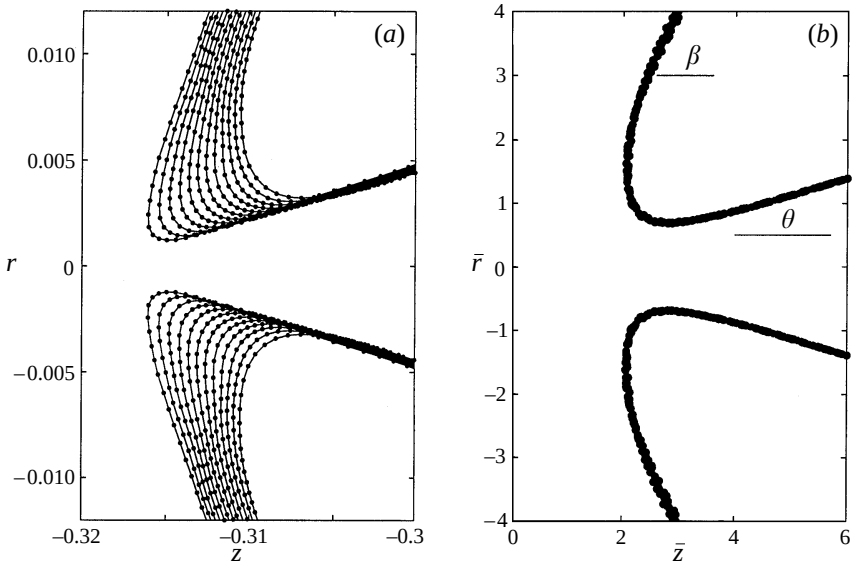

FIGURE 10. Self-similar regime. (*a*) Surface evolution in the primitive coordinates. (*b*) Surface shape in the normalized coordinates (see text). Data for $\tau < 0.004$. Solid circles represent grid points.

slice model or any one-dimensional model will be inappropriate. The fold-over allows the curvature κ_1 to catch up to the slowing κ_2. There is a cross-over as they mutually approach the 2/3 growth rate. Folding is the mechanism by which the system reconciles the high pressures within the jetting bubble and the low pressure outside. Fold-over is due to strong axial fluid motion at the neck.

9. Self-similarity

Figure 10(*b*) plots the shapes after fold-over ($\tau < 0.004$) using the similarity variables,

$$\bar{r} \equiv r/\tau^{2/3}, \quad \bar{z} \equiv (z - z_p)/\tau^{2/3}. \tag{9.1}$$

There is a clear collapse of the data. The interface collapses with a far-field shape of two cone-like surfaces with angles $\theta \approx 12^\circ$ and $\beta \approx 53^\circ$ (apex at the singular point). The minimum point has the velocities

$$\left.\frac{\mathrm{d}z}{\mathrm{d}t}\right|_{r_{min}} = -\tfrac{2}{3}(\bar{z}_{min})\,\tau^{-1/3}, \qquad \left.\frac{\mathrm{d}r}{\mathrm{d}t}\right|_{r_{min}} = -\tfrac{2}{3}(\bar{r}_{min})\,\tau^{-1/3}.$$

Here $\bar{r}_{min} \approx 0.67$ and $\bar{z}_{min} \equiv \bar{z}|_{\bar{r}_{min}} \approx 2.7$, which can be read directly from figure 10(*b*). In addition to the collapse of data, illustrated in figures 10–12, the curves formed by the collapsed data have been independently verified as solutions of the similarity equations ((9.2), (9.3) below).

The scaled curvatures and their sum are plotted against arclength in figure 11. Arclength increases with increasing z, that is from left to right in the plot of normalized shape (figure 10*b*). In figure 11(*a*), consider passing around the fold from the converging flow within the forming bubble to the diverging region outside (decreasing $\bar{s}$). Curvature $\bar{\kappa}_1$ first drives the pressure up in the direction of the neck while its partner $\bar{\kappa}_2$ restrains the growth of the mean curvature by an increase in the opposite

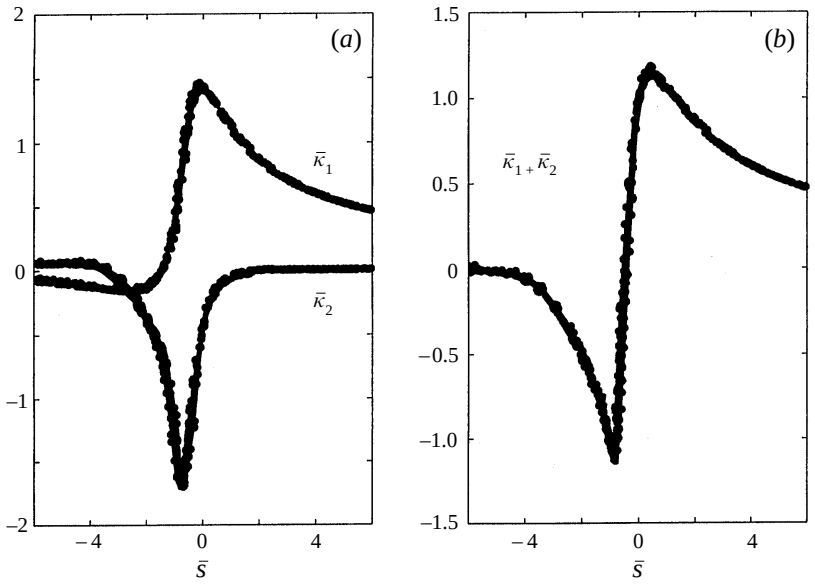

FIGURE 11. Self-similar regime. (*a*) Rescaled principal curvatures and (*b*) rescaled mean curvature. Solid circles represent grid points.

sense. The growth of $\bar{\kappa}_2$ lags behind. As the neck is passed, $\bar{\kappa}_2$ eventually overcomes its partner and then relaxes as the fold is rounded. $\bar{\kappa}_1$ and then $\bar{\kappa}_2$ each pass through zero, switching signs, to give a mean curvature that approaches zero. The mean curvature plot (figure 11*b*) shows how the self-similar fold allows the curvature to jump from order one to near zero. This is a shock in mean curvature. It arises in response to the pressure jump that occurs at an orifice emptying into a reservoir. The rescaled velocities $\bar{v}_s \equiv \bar{\boldsymbol{v}}\cdot\boldsymbol{s}$ and $\bar{v}_n \equiv \bar{\boldsymbol{v}}\cdot\boldsymbol{n}$ are plotted versus arclength in figure 12(*a*, *b*), respectively. They show a similar shock-like structure. The dipole distribution $\bar{\mu}$ is plotted in figure 12(*c*).

The equations governing the self-similar regime are obtained by rescaling the primary variables $(t, r, z) \mapsto (\tau, \bar{r}, \bar{z})$ as given by (1.2) and (9.1). The transformations $(s, \mu, \boldsymbol{v}, \kappa_1, \kappa_2) \mapsto (\bar{s}, \bar{\mu}, \bar{\boldsymbol{v}}, \bar{\kappa}_1, \bar{\kappa}_2)$ are also used, as inherited in a straightforward way from the primary rescaling. Steady solutions of the transformed equations are of interest ($\partial/\partial\tau = 0$). The corresponding kinematic condition and the Bernoulli–Laplace equation for the similarity behaviour are written, respectively (dropping overbars hereafter),

$$v_n = \tfrac{2}{3}(r'z - z'r), \tag{9.2}$$

and

$$-\tfrac{1}{3}\mu + \tfrac{2}{3}(zz' + rr')\mu' + v_s\mu' = -(\kappa_1 + \kappa_2). \tag{9.3}$$

The first two terms on the left of (9.3) represent acceleration, the third term kinetic energy, and the right-hand side the jump in pressure. The original PDE system is replaced by this pair of ordinary differential equations coupled through (3.5).

Salient behaviour of solutions to the similarity equations (9.2), (9.3) is deduced through an approximation that we shall refer to as the *conical flow approximation.* Figure 10(*b*) suggests a far-field, nearly conical interface, idealized in figure 13(*a*), according to which $\kappa_1 \sim \cot\theta/s$ for the θ-cone and $\kappa_1 \sim \cot\beta/s$ for the β-cone and $\kappa_2 \approx 0$ for both cones. Consistent with this geometry is $v_n \approx 0$ and a nearly

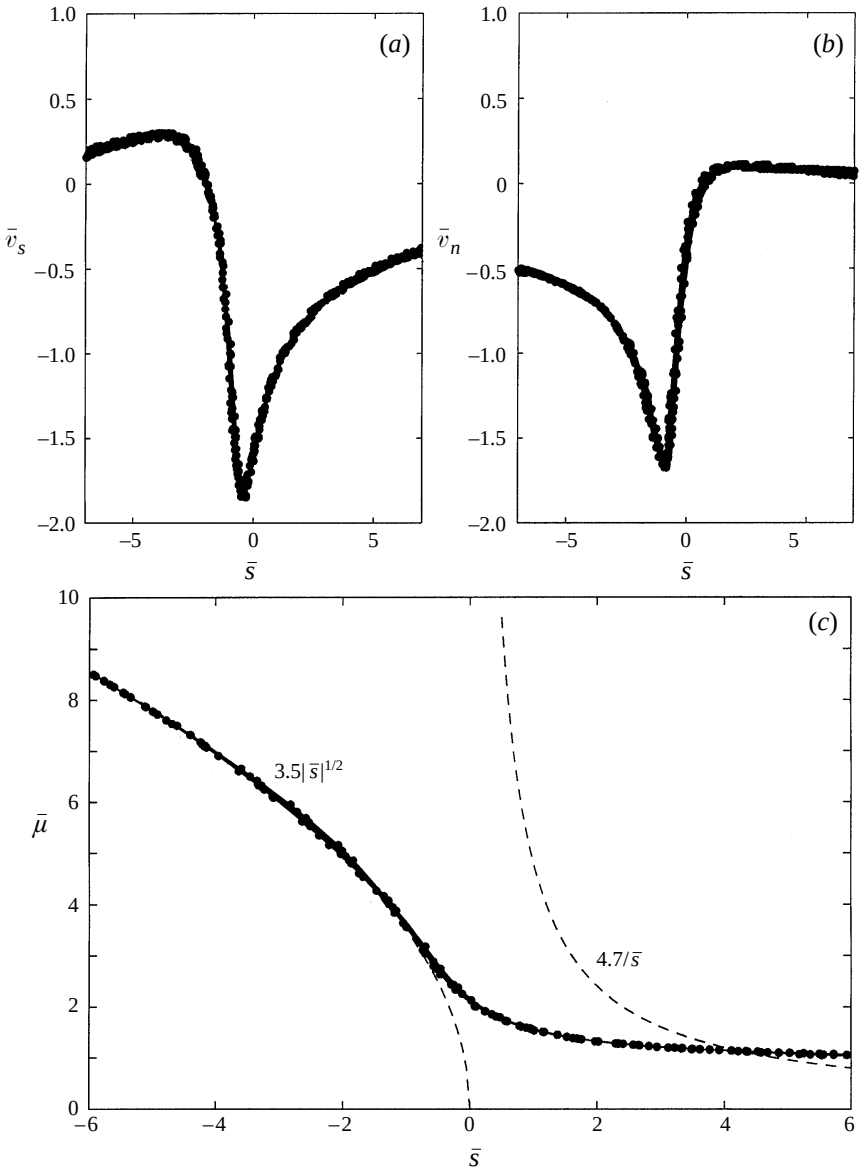

FIGURE 12. Self-similar regime. Rescaled (*a*) tangential and (*b*) normal velocity distribution. (*c*) Rescaled dipole distribution function. Solid circles represent grid points.

radial flow, converging in region A and diverging in region C. Within the conical wedge region B, where there is no net flow across any spherical sector, the motion is relatively weak. The slenderness of region A makes an approximation based on a one-dimensional slice model appropriate (Ting & Keller 1991):

$$\left.\begin{aligned} r &\sim c_0 z - \tfrac{3}{4} c_0 c_1 z^{-1/2}, \\ v_s &\sim -c_1 z^{-1/2} - \left(\frac{1}{c_0} + \frac{c_1^2}{2}\right) z^{-2}, \quad z \gg 1. \end{aligned}\right\} \tag{9.4}$$

Here $c_0 = \tan\theta$ consistent with a conical far-field interface. Note, however, that the

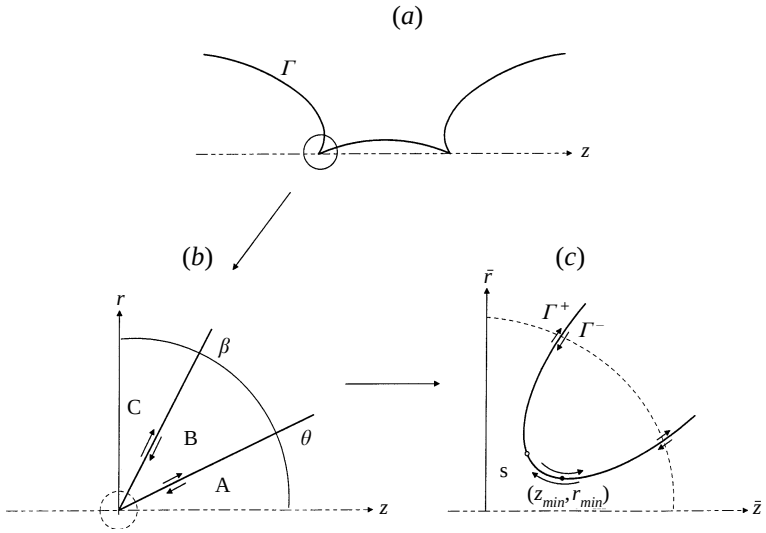

FIGURE 13. A schematic of the flow near pinchoff from (*a*) perspective of the whole bridge, (*b*) far field of one pinch point, and (*c*) close to the singularity in the scaled coordinates. The point denoted 's' in (*c*) is the stagnation point. See text for other nomenclature.

modification to the conical interface (c_1 term) gives the dominant far-field decay of v_s. The implied $s^{-1/2}$ decay is reasonably confirmed in figure 12(*a*).

In the conical-flow approximation, the only balance left to satisfy is (9.3), which reduces to an ODE for μ, inhomogeneous with variable coefficients. The v_s coefficient (order $s^{-1/2}$) is small in comparison to the acceleration coefficient (order s) and hence can be neglected, leaving

$$-\tfrac{1}{3}\mu + \tfrac{2}{3}s\mu' = \begin{cases} -\cot\theta/s & \text{for } s \gg 1 \\ -\cot\beta/s & \text{for } s \ll -1. \end{cases} \tag{9.5}$$

Since the acceleration must feature in any balance, only two dominant balances are possible: (i) acceleration balances pressure or (ii) the two acceleration contributions balance one another. Balance (i) is appropriate on the converging side where surface tension drives the flow and balance (ii) is appropriate on the diverging side where flow relaxes. Straightforward solution of (9.5) yields in these cases,

$$\text{(i)} \quad \mu \sim a^+/s \quad \text{on converging side} \quad (s \to +\infty),$$

$$\text{(ii)} \quad \mu \sim a^-|s|^{1/2} \quad \text{on diverging side} \quad (s \to -\infty).$$

The solution shows that a^+ is equal to $\cot\theta$. Coefficient a^- can only be determined by matching. Accordingly, the far-field solution (9.4) has c_1 correlated with a^-.

Key characteristics of the solution to (9.2), (9.3), as obtained from the direct computations, are listed in table 2 for reference. The conical flow approximation can be checked against computation. The deviation of v_n from $v_n = 0$ is slight on the converging cone but striking on the diverging cone (figure 12*b*). The velocities (v_n, v_s) are expected to decay as $s^{-1/2}$ in the far field of cone A according to (9.4). Velocities in cone C are also expected to decay as $s^{-1/2}$ since they are related non-locally (by integration through (3.5)) to those in cone A. Any deviation from these decay rates (figure 12*a*, *b*) is probably due to the limited extent of the self-similar region. That is, one would have to calculate an order of magnitude or so further in τ for the far

t_p	4.37329	z_p	0.32
$\bar{r}_{min}$	0.67	$\bar{z}_{min}$	2.7
θ	12°	β	53°
a^+	4.7	a^-	3.5
$\|\kappa_1\|_{max}$	1.5	$\|\kappa_2\|_{max}$	1.7

TABLE 2. Characteristics of the similarity solution before breakup near the the pinchoff point according to computation. The numbers $a^{\pm}$ stand for the asymptotic behaviour of the dipole distribution where a^- is the best fit and $a^+ = \cot\theta$; see figure 12(*c*).

Onset	Roll-off	Cusp-approach	Self-similar
$\Delta r \propto t^2$	$r \propto \tau^{2/3}$	$(r,z) \propto (\tau^{2/5}, \tau^{3/5})$	$(r,z) \propto (\tau^{2/3}, \tau^{2/3})$
$t \ll 1$	$0.04 < \tau < 0.4$	$0.004 < \tau < 0.04$	$\tau < 0.004$

TABLE 3. Regimes and relevant time scales during the breakup of the film bridge.

field of the self-similar region to fully reveal itself. The same comment applies to the asymptotic behaviour of the potential which is compared to the computations in figure 12(*c*). In summary, the conical flow approximation seems to capture the far-field behaviour to the extent that it is revealed.

In summary, solutions to the self-similar problem are characterized by three parameters $\{\theta, \beta, a^-\}$. The sense in which our computational solution is 'universal' will depend on the relationship of the self-similar problem to the initial-value problem. The matching and constraints that determine these three parameters (and this relationship) are beyond our scope.

10. Concluding remarks

We study an example where an inviscid flow interacts with its deforming container. The surface drives the flow which in turn modifies the final deformation of the surface as it approaches pinchoff.

The evolution shows a sequence of regimes beginning from the initial growth of the disturbance at the neutrally stable steady catenoid and ending at the pinch instant. Table 3 summarizes these regimes indicating the scaling exhibited and the corresponding duration. After onset and roll-off the primary neck decelerates due to the stagnation point in the flow field at mid-axis to form a primary satellite bubble. Two secondary necks take over the collapse process and do not produce satellite bubbles because of the jetting rather than stagnation flow at the pinch points. That is, the underlying flow field at mid-axis has different symmetry from that at the twin pinch points. Up to and including cusp approach, the axial flow dominates and one-dimensional flow approximation is reasonable. Beyond cusp approach, with fold-over, flow in the radial direction and reverse axial flow become important. Figure 13 sketches the self-similar geometry at pinchoff, figure 13(*c*) showing an expanded view of the apex in figure 13(*b*). The 'stagnation point' on the interface ($v_s = 0$) is located in figure 13(*c*). At this point, the tangential velocities across the interface are equal and opposite to one another. That is, downstream, the flow on Γ^- is stronger than on Γ^+ while the reverse it true upstream.

The finite-time singularity that ultimately develops follows a 2/3 power law, as predicted by dimensional analysis. The axial acceleration of the fluid located at the

pinch point at the pinch instant balances the net axial surface tension force of the conical-wedge configuration. It is this axial acceleration and its ramifications that are likely to show up in any experiment for which the flow is inviscid over much of the collapse.

This work was supported in part by NASA NAG3-801 and NAG3-1854.

The data of figure 7 were taken by Dr Brian Lowry. Measurement of bubble diameter as a function of ring diameter were performed by Kara Gaetano and Laura Woeller. P.H.S. would like to acknowledge useful discussions on various aspects of this problem with Dr E. Meiburg, Dr J. Hinch, Dr J. Lister and Mr R. Day. Work on this paper by P.H.S. took place during a sabbatic leave. He would like to thank Dr T. Coleman (ACRI, Cornell University), Dr-Ing. U. Mueller and Dr-Ing. P. Ehrhard (IATF, Forschungszentrum Karlsruhe) and Dr M. G. Worster (DAMTP, Cambridge University) for their respective generous hospitalities. Partial support also came from the Alexander von Humboldt foundation.

This research was conducted using the resources of the Cornell Theory Center, which receives major funding from the National Science Foundation and New York State with additional support from the Advanced Research Projects Agency, the National Center for Research Resources at the National Institutes of Health, IBM Corporation and members of the Corporate Research Institute.

REFERENCES

Baker, G. R. Meiron, D. I. & Orszag, S. A. 1982 Generalized vortex methods for free-surface flow problems. *J. Fluid Mech.* **123**, 477.

Bliss, G. A. 1946 *Lectures on the Calculus of Variations*. University of Chicago Press.

Chaudhary, K. C. & Redekopp, L. G. 1980 The nonlinear capillary instability of a liquid jet. Part 1. Theory. *J. Fluid Mech.* **96**, 254.

Chopp, D. L. & Sethian, J. A. 1991 Flow under mean curvature: singularity formulation and minimal surfaces. *Rep.* 541. Center for Pure and Applied Mathematics, University of California Press.

Cryer, S. A. 1990 Equilibrium shapes and rupture dynamics of a soap-film bridge. PhD dissertation, Cornell University.

Cryer, S. A. & Steen P. H. 1992 Collapse of the soap-film bridge: quasistaic description. *J. Colloid Interface Sci.* **154,** 276.

Dussan V., E. B. 1975 Hydrodynamic stability and instability of fluid systems with interfaces. *Arch. Rat. Mech. Anal.* **57**, 363.

Eggers J. 1993 Universal pinching of 3D axisymmetric free surface flow. *Phys. Rev. Lett.* **71,** 3458.

Eggers J. & Dupont, T. F. 1994 Drop formation in a one-dimensional approximation of the Navier–Stokes equation. *J. Fluid Mech.* **262**, 205.

Euler, L. 1744 Opera Omnia (Orell Fussli), **24**(1), 25.

Gillete, R. D. & Dyson, D. C. 1971 Stability of fluid interfaces of revolution between equal solid circular plates. *Chem. Engng J.* **2**, 44.

Gray, L. J. & Sansoucie, C. 1993 A Hermite interpolation algorithm for hypersingular boundary integrals. *Int. J. Numer. Meth. Engng* **36**, 2357.

Hadamard, J. 1923 *Lectures on Cauchy's Problem in Linear Partial Differential Equation.* Yale University Press.

Hou, T. Y., Lowengrub J. S. & Shelly M. J. 1994 Removing the stiffness from interfacial flow with surface tension. *J. Comput. Phys.* **114**, 312.

Howe, W. 1887 Die Rotations–Flächen welche bei vorgeschriebener Flächen-grösse ein möglichst grosses oder kleines Volumen enthalten. PhD dissertation, Friedrich-Wilhelms Universität zu Berlin.

Keller, J. B. 1983 Breaking of liquid films and threads. *Phys. Fluids* **26**, 3451.

Keller, J. B., King, A. & Ting, L. 1995 Blob formation. *Phys. Fluids* **7**, 226.

Keller, J. B. & Miksis, M. J. 1983 Surface tension driven flows. *SIAM J. Appl. Maths* **43**, 268.

Krishnasamy, G., Schmerr, L. W., Rudolphi, T. J. & Rizzo, F. J. 1990 Hypersingular boundary integral equations: some applications acoustic and elastic wave scattering. *J. Appl. Mech.* **57**, 404.

Lamb, H. 1932 *Hydrodynamics*, 6th edn. Cambridge University Press.

Lowry, B. J. & Steen P. H. 1995 Capillary surfaces: stability from families of equilibria with application to the liquid bridge. *Proc. R. Soc. Lond.* A **449**, 411.

Maddocks, J. H. 1987 Stability and folds. *Arch. Rat. Mech. Anal.* **99**, 301.

Mansour, N. & Lundgren, T. S. 1990 Satellite formation in capillary jet breakup. *Phys. Fluids* A **2**, 1141.

Meseguer, J. 1983 The breaking of axisymmetric slender bridges. *J. Fluid Mech.* **130**, 123.

Papageorgiou, D. T. 1995*a* Analytical description of the breakup of liquid jets. *J. Fluid Mech.* **301**, 109.

Papageorgiou, D. T. 1995*b* Study of cylindrical jet breakup using one-dimensional approximations of the Euler equations. Preprint.

Peregrine, D. H., Shoker, G. & Symon, A. 1990 The bifurcation of liquid bridges. *J. Fluid Mech.* **212**, 25.

Plateau, J. A. F. 1863–1866 Experimental and theoretical researches on the figures of equilibrium of a liquid mass. Translated in *Ann. Rep. Smithsonian Institution.*

Pozrikidis, C. 1992 *Boundary Integral and Singularity Methods for Linearized Viscous Flow*. Cambridge University Press.

Schulkes, R. M. S. M. 1993 Dynamics of liquid jets revisited. *J. Fluid Mech.* **250**, 635.

Shi, X. D., Brenner, M. P. & Nagel, S. R. 1994 A cascade of structure in a drop falling from a faucet. *Science* **265**, 219.

Steen, P. H. 1992 Capillary containment and collapse in low gravity: dynamics of fluid bridges and columns. In *Free Boundary Problems: Theory and Applications.* Longman-Pitman Publishing.

Ting, L. & Keller, J. B. 1990 Slender jets and thin sheets with surface tension. *SIAM J. Appl. Maths* **50**, 1533.

Tjahjadi M., Stone, H. A. & Ottino, J. M. 1992 Satellite and subsatellite formation in capillary breakup. *J. Fluid Mech.* **243**, 297.